Electronic Supplementary Material (ESI) for Materials Horizons.
This journal is © The Royal Society of Chemistry 2023

Supporting Information

Patterned liquid metal embedded in brush-shaped polymer for dynamic thermal management

Qingxia He, Mengmeng Qin, Heng Zhang, Junwei Yue, Lianqiang Peng, Gejun Liu, Yiyu Feng, Wei Feng**

School of Materials Science and Engineering and Tianjin Key Laboratory of Composite and Functional Materials, Tianjin University, Tianjin 300350, P. R. China

Email: weifeng@tju.edu.cn (Wei Feng); qmm@tju.edu.cn (Mengmeng Qin)

S: Supporting information

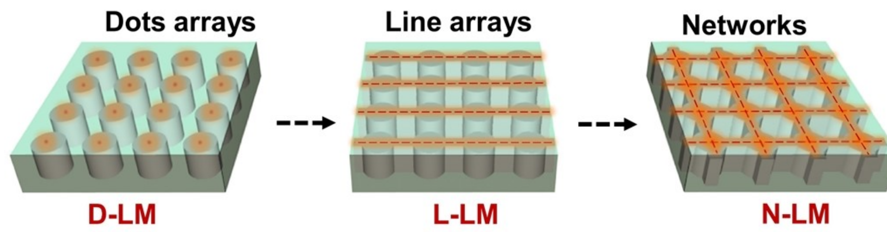

Fig. S1. Schematic diagram of LM paths, including dots arrays, lines, and networks.

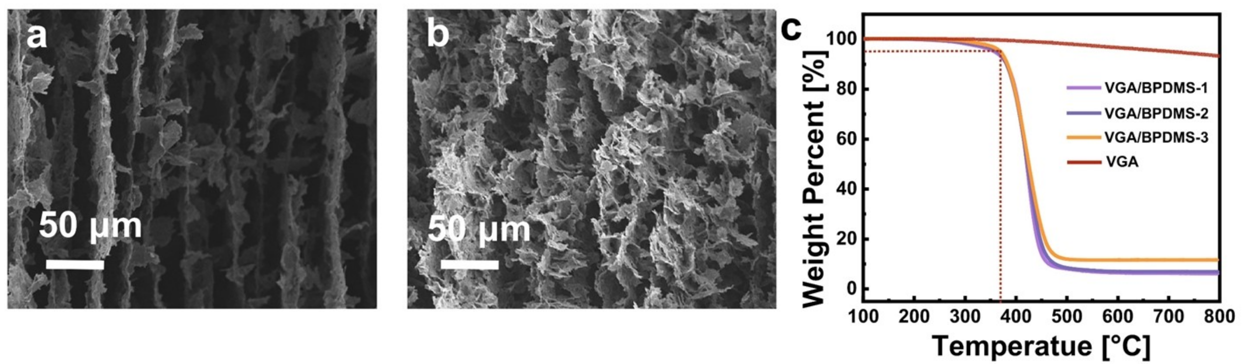

Fig. S2. (a-b) The cross section SEM images of VAG with different density. (c) The thermogravimetric analysis (TGA) results of VGA and VGA/BPDMS composite with different filler loading.

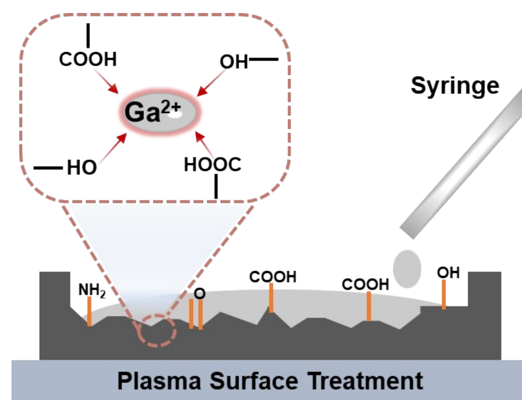

Fig.S3. The illustration of plasma treatment of substrate surface to increase compatibility between material and liquid metal.

Table S1. Recipe for fabrication of soft PDMS elastomers presented as molar ratio of each polymer component. Equilibrium shear storage modulus is taken as the measured value at oscillatory frequency of 0.01 Hz, temperature of 25 °C, and fixed strain of 0.5%.

Sample name	Molar ratio (Crosslink chains/Side chains)	Shear storage modulus (Pa)	Gel fraction (wt%)
BPDMS-0	0	1649.4	62.5
BPDMS-10^{-3}	10^{-3}	4006.9	68.3
BPDMS-10^{-2}	10^{-2}	7009.2	77.1
BPDMS-10^{-1}	10^{-1}	32352	80.0
Sylgard®184 (10:1)	-	49371	95.9
Sylgard®184 (50:1)	-	3925.6	53.4

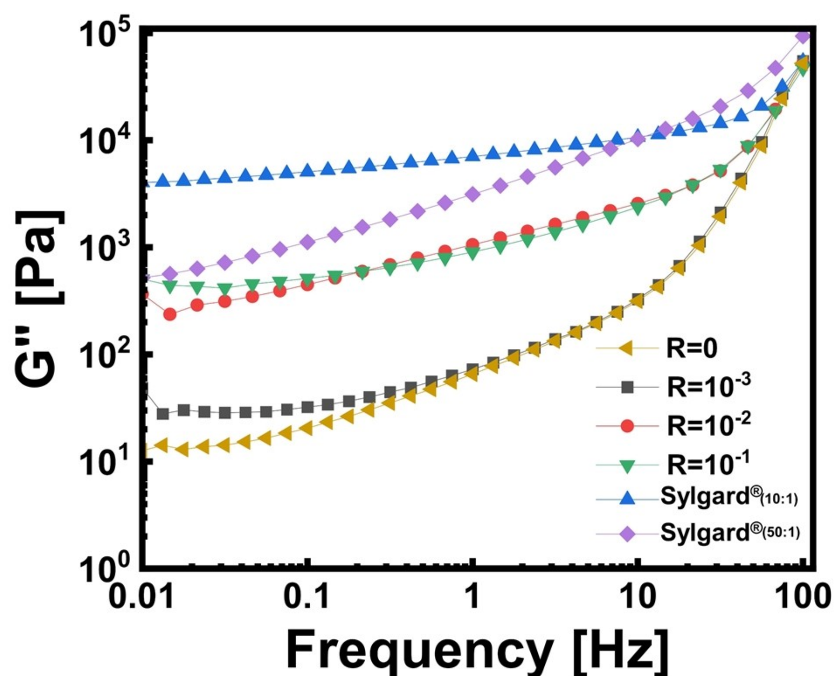

Fig. S4. Frequency dependence of the shear loss modulus (G″) of BPDMS and Sylgard® 184 measured at 20 °C at a fixed strain of 0.5%.

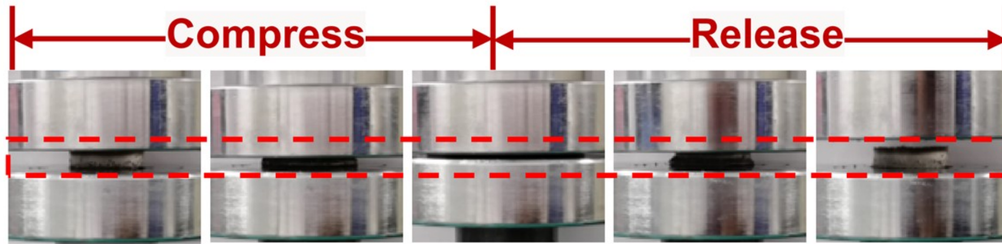

Fig. S5. The optical images of conpress-release process of BPDMS.

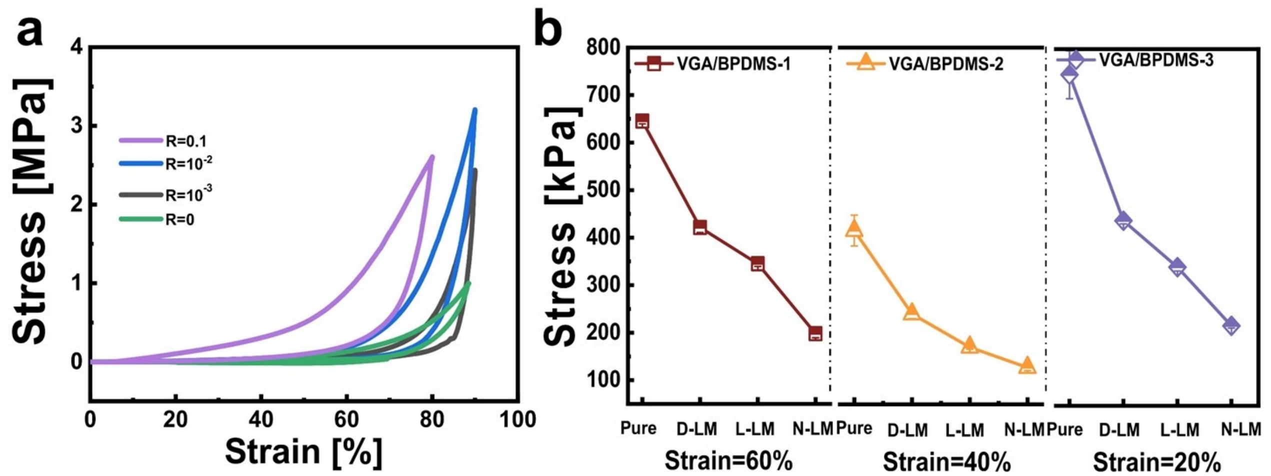

Fig. S6. (a) The strain-stress curves of brush-shaped PDMS with different molar ratio of crosslink chain and side chain. (b) The summery of compressibility performances of the VGA/BPDMS and LM-VGA/BPDMS composites with different LM patterns and VGA loading.

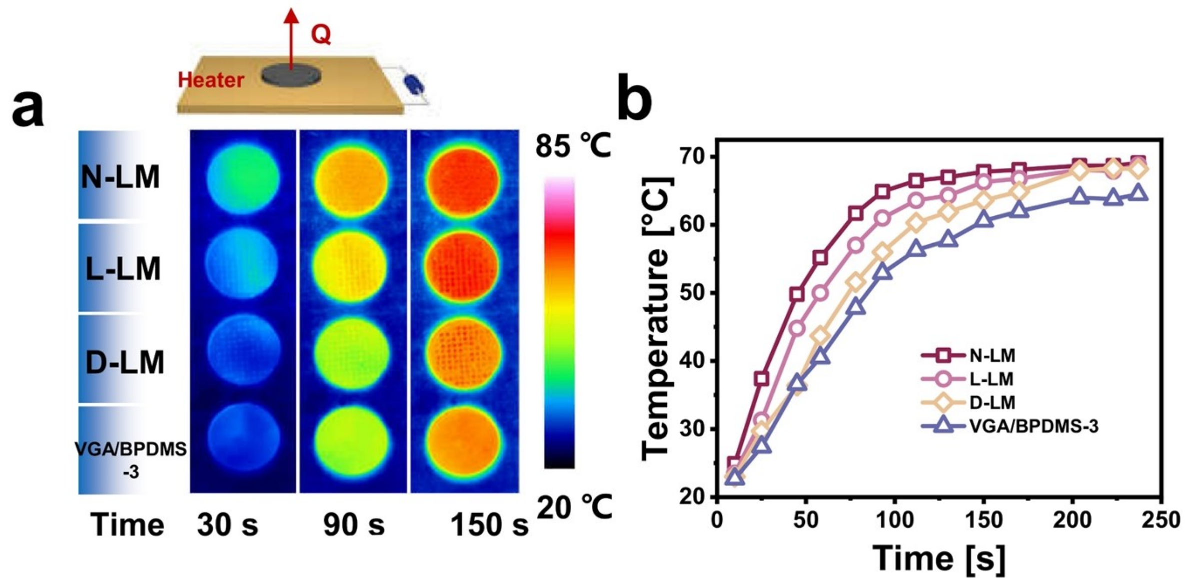

Fig. S7. (a) IR camera images showing the temperature distribution on N-LM/BPDMS-3, L-LM-VGA/BPDMS-3, D-LM/VGA/BPDMS-3 and VGA/BPDMS-3 at different times. (b) Evolution of the maximum surface temperature with heating time.

Figure S7a-b revealed the surface temperature evolution of four composites as a function of heating time. The heat transfer rate of N-LM-VGA/BPDMS-3 displayed a slope of 1.12, higher than those of other LM -VGA/BPDMS with different LM patterns and VGA/BPDMS-3, respectively, which is consistent with the increasing trend of $\kappa_{\perp}$ for these three samples [c.f. Figure 2a, N-LM-VGA/BPDMS-3 ($\kappa_{\perp}$ = 7.11 $Wm^{-1}K^{-1}$) > L-LM-VGA/BPDMS-3 ($\kappa_{\perp}$ = 6.29 $Wm^{-1}K^{-1}$) > D-LM/BPDMS-3 ($\kappa_{\perp}$ = 3.74 $Wm^{-1}K^{-1}$)>VGA/BPDMS-3 ($\kappa_{\perp}$ = 2.82 $Wm^{-1}K^{-1}$)]. This trend explains why the N-LM-VGA/BPDMS-3 sample reached a higher maximum temperature than that of other developed materials.

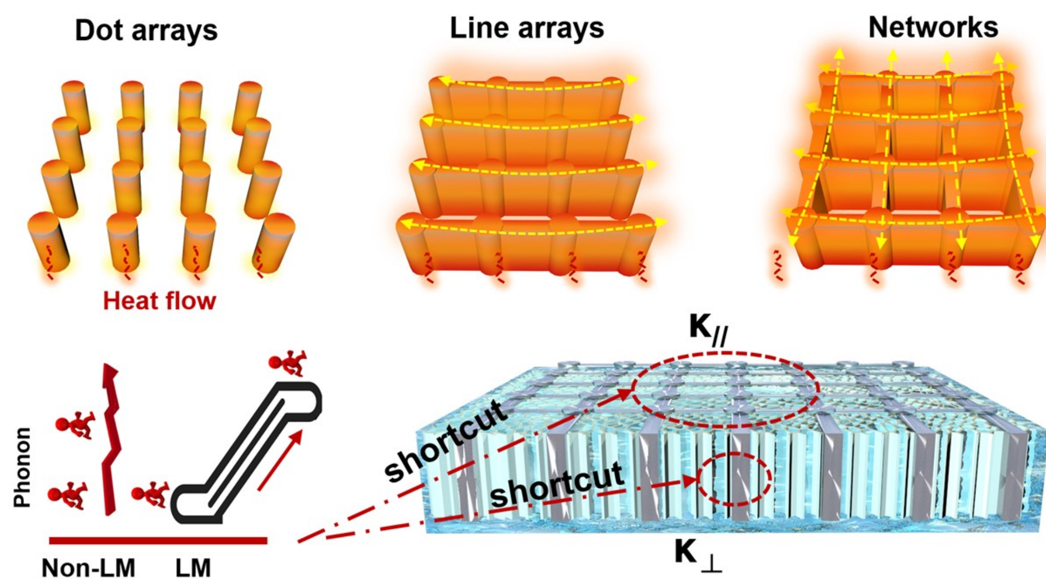

Fig. S8. The Mechanism of enhancing thermal conductivity through bicontinuous networks.

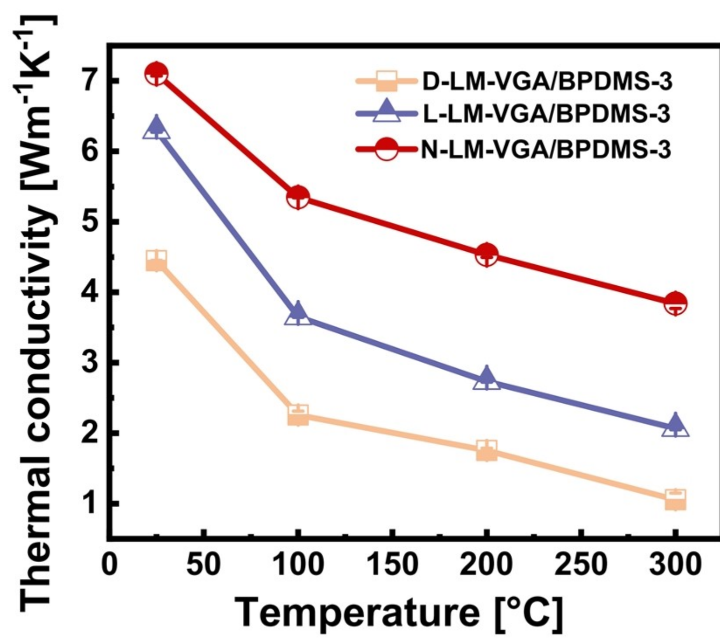

Fig. S9. The thermal conductivity of LM-VGA/BPDMS composites materials declined with the increasing of temperature.

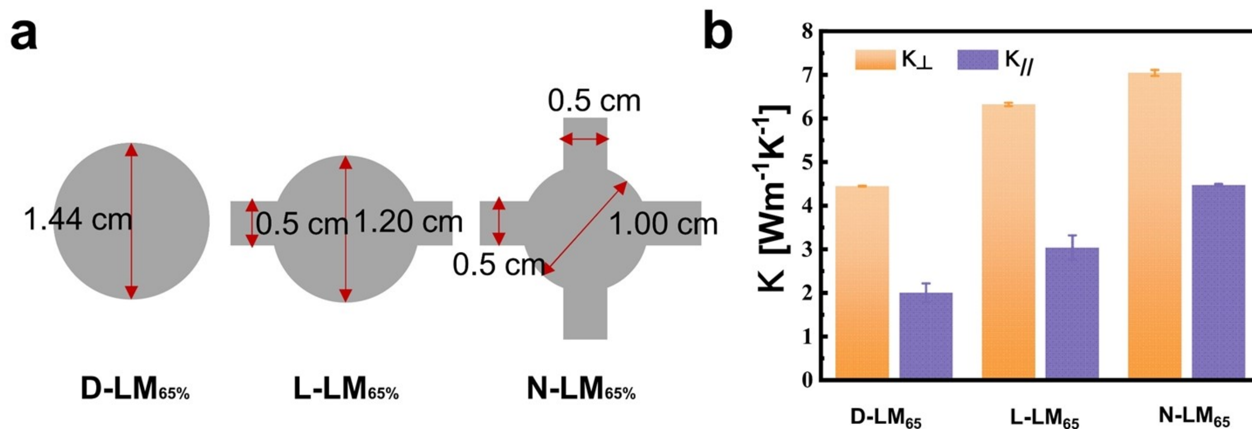

Fig. S10. (a) The parameters of three patterned different thermal conductive pathways. (b) The thermal conductivity of LM_{65}-VGA/BPDMS-3 with different patterns at the same LM loading.

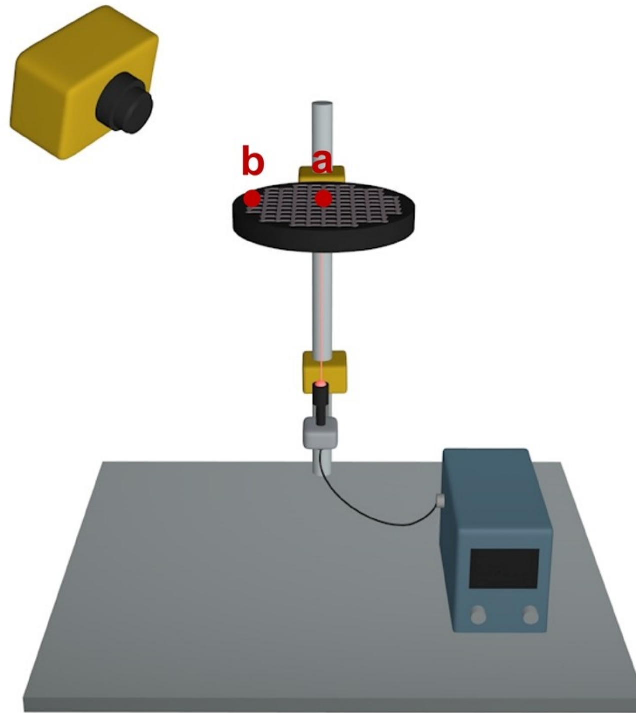

Fig. S11. The schematic diagram of the laser-thermal IR imaging experiment to intuitively observe the in-plane heat transfer of point heat sources within N-LM-VGA/BPDMS composites.

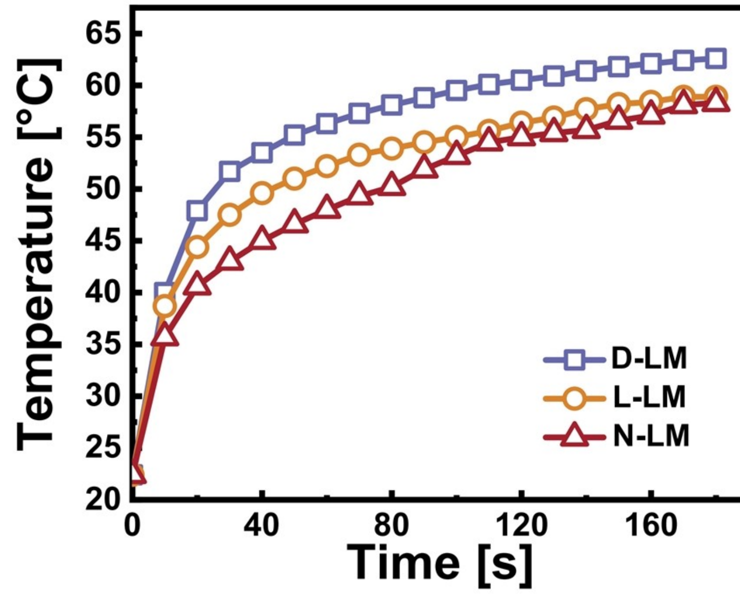

Fig. S12. Evolution of surface temperature at points marked by point “a”.

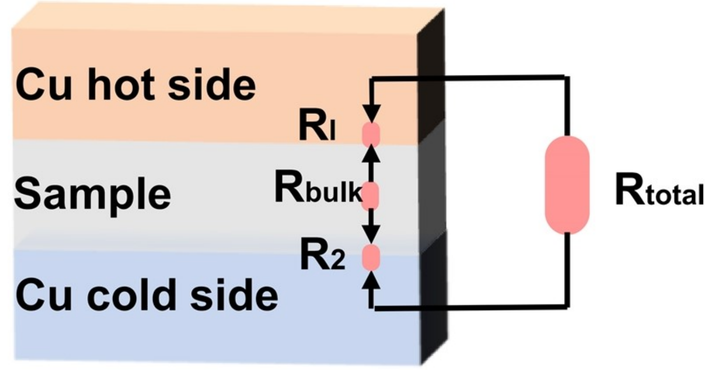

Fig. S13. An illustration indicating how to calculate the thermal contact resistance of samples. The contact thermal resistance (R_c) of the sample can be calculated by following equations: [R1-R2]

$$R_c=R_1+R_2$$

$$R_{total}=R_{bulk}+R_c=BLT/k_{eff}$$

$$R_{bulk}=BLT/k_{bulk}$$

where R_{total} is the total resistance of the interface between two copper plates, R_{bulk} is the intrinsic thermal resistance of the sample, R_c is the thermal contact resistance between the sample and the double sides, BLT is the bond line thickness, k_{eff} is the effective thermal conductivity of the sample, k_{bulk} is the intrinsic thermal conductivity of the samples. The samples were sandwiched between two pieces of copper plates with applying the pressure of 40 kPa. The thermal conductivity of samples was measured based on ASTM D5470 by the DRL-III instrument (Xiangtan Xiang Yi Instrument, Ltd., China). BLT was obtained by measure the thickness of the samples when used under packaging conditions.

Table S2. The calculated thermal contact resistance (R_c) of the applied thermal conductive materials

	BLT (mm)	k_{bulk} ($Wm^{-1}K^{-1}$)	R_{bulk} (Kmm^2W^{-1})	k_{eff} ($Wm^{-1}K^{-1}$)	R_{total} (Kmm^2W^{-1})	R_c (Kmm^2W^{-1})
N-LM-VGA/BPDMS-1	3050	1.44	2118.0	1.32±0.006	2298.4±9.95	180.37±9.95
N-LM-VGA/BPDMS-2	2853	4.42	645.5	4.325±0.007	659.65±1.08	14.16±1.08
N-LM-VGA/BPDMS-3	2850	7.11	400.84	6.23±0.05	457.57±3.7	56.73±3.7

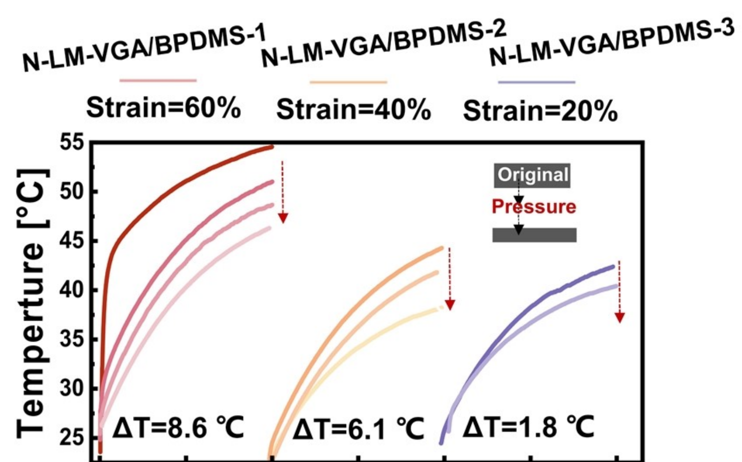

Fig. S14. Real-time cooling performance of N-LM-VGA/BPDMS with different VGA contents and compression ratios.

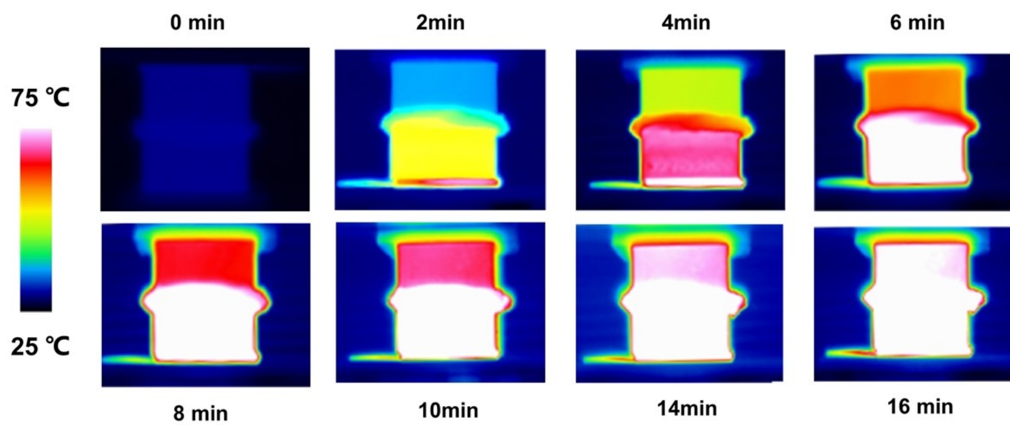

Fig. S15. The infrared thermographs of the elastic N-LM-VGA/BPDMS-2 composite sandwiched in wavy surface with heating time.

Through an infrared temperature detector, we could more intuitively observe the heat transfer ability of the elastic thermal conductor interface, as shown in **Figure S15**. With the passage of time, the temperature of the upper surface gradually increased, and after 14 minutes, the upper and lower surface temperatures tended to be consistent, indicating that N-LM-VGA/BPDMS can effectively transfer heat between the upper and lower surfaces.

Table S3. The materials parameters used in the thermal-mechanical simulation.

Description	Value	unit
Specific heat capacity (N-LM/VGA/BPDMS)	1100	J/(kg·K)
Density (N-LM/VGA/BPDMS)	2300	Kg/m^3
Thermal conductivity (N-LM/VGA/BPDMS)	4.46	W/(mK)
Specific heat capacity (Copper)	386	J/(kg·K)
Density (Copper)	8900	Kg/m^3
Thermal conductivity (Copper)	400	W/(mK)
Young's modulus	23130	Pa
Poisson's ratio	0.4	1

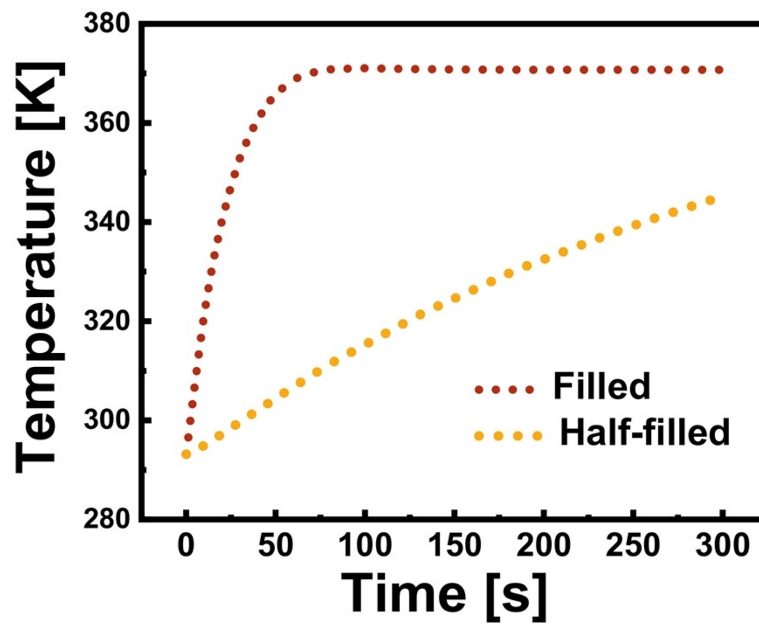

Fig. S16. Evolution of surface temperature at points marked by point "a".

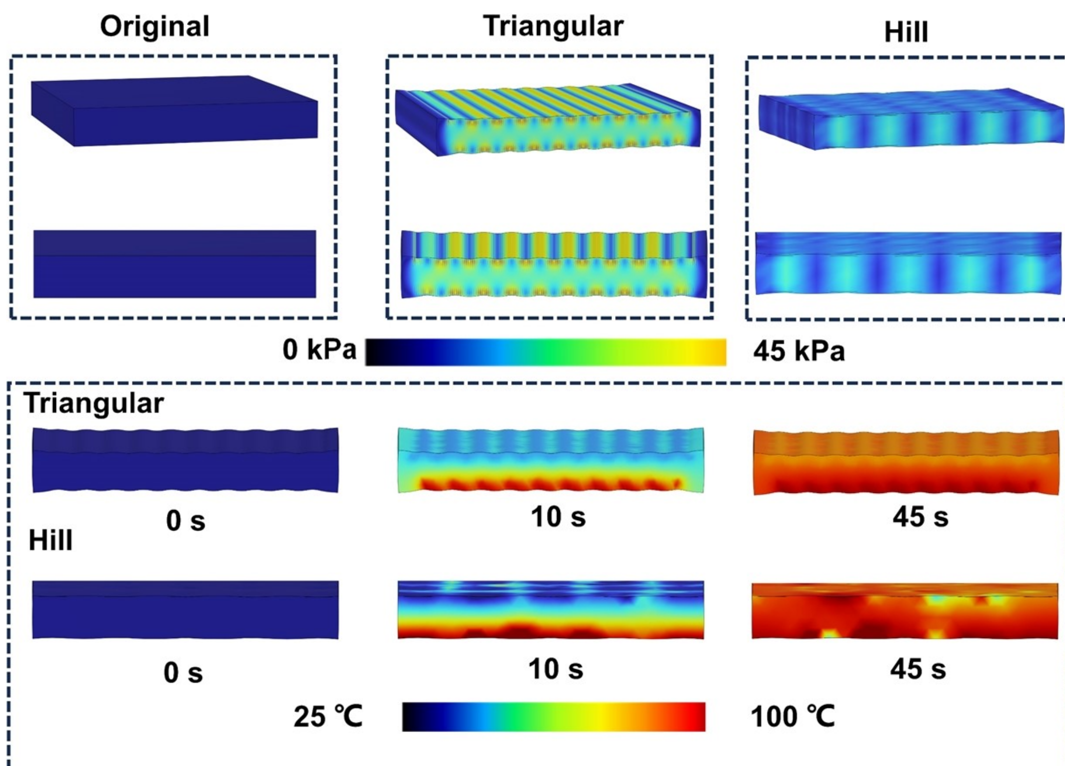

Fig. S17. Finite element analysis about temperature and stress distribution of N-LM-VGA/BPDMS when fully filled into triangular and hill interfaces.

Fig. S18. The optical images of the dynamic thermal sensing temperature detection equipment.

REFERENCES

[R1] C. Guo, Y. Li, J. Xu, Q. Zhang, K. Wu, Q. Fu, *Mater. Horiz.* **2022**, 9, 1690.
[R2] H. Zhang, Q. He, H. Yu, M. Qin, Y. Feng, W. Feng, *Adv. Funct. Mater.* **2023**, 33, 2211985.